Flow (2023), **3** E32
doi:10.1017/flo.2023.26

FLOW CAMBRIDGE UNIVERSITY PRESS

RESEARCH ARTICLE

Proper orthogonal decomposition modal analysis in a baffled stirred tank: a base tool for the study of structures

Arturo A. Arosemena[1],* and Jannike Solsvik[1]

[1]Department of Chemical Engineering, Norwegian University of Science and Technology (NTNU), NO-7491 Trondheim, Norway
*Corresponding author. E-mail: arturo.arosemena@ntnu.no

Received: 12 December 2022; **Revised:** 25 July 2023; **Accepted:** 24 August 2023

Keywords: Turbulent flows; Mixing and mixers

Abstract

Proper orthogonal decomposition (POD) is applied to three-dimensional (3-D) velocity fields collected from large-eddy simulations (LES) of a baffled stirred tank. In the LES, the tank operates with a Rushton-type impeller under turbulent conditions (at least in the near-impeller region) and the working fluid exhibits either Newtonian or shear-thinning rheology. The most energetic POD modes are analysed, and a POD reconstruction based on the higher modes is proposed to approximate the fluctuating component of the velocity field. Subsequently, the POD reconstruction is used to identify vortical structures and characterise them in terms of their shape. The structures are identified by considering a frame-invariant formulation of a popular, Eulerian, local-region-type method: the Q-criterion. Statistics of shape-related parameters are then investigated to address the morphology of the structures. It is found that: (i) regardless of the working fluid rheology, it seems feasible to decompose the 3-D field into its mean, most energetic periodic and fluctuating components using POD, allowing, for instance, reduced-order modelling of the energetic periodic motions for mixing enhancement purposes, and (ii) vortical structures related to turbulence are mostly tubular. Finding (ii) implies that, as starting point, phenomenological models for the interaction between fluid particles (drops and bubbles) and vortices should consider the latter as cylindrical structures rather than of spherical shape, as classically assumed in these models.

Impact Statement

Stirred tank reactors are used for homogenisation, interphase mass transfer and chemical reactions in numerous industries. Therefore, there is a persistent need for improving their performance. In this sense, one possibility is to work towards more optimal designs. Another is to take full advantage of the current ones. In any case, it is critical to have a better understanding of the flow in stirred tanks, which is quite complex, particularly in the case of turbulence. This paper considers a linear technique (proper orthogonal decomposition) to decompose three-dimensional instantaneous velocity fields obtained from numerical simulations (large-eddy simulations), with the aim of exploring the most energetic motions and related structures (coherent regions in time and/or space). The findings herein can guide future efforts to make the most of the energetic regions in the flow and also provide a basis for more realistic models to address turbulence–fluid-particles (drops and bubbles) interactions.

1. Introduction

Stirred tanks are mechanically agitated vessels, used for mixing enhancement purposes, encountered in almost 25 % of all operations in the process industry (Nikiforaki, Montante, Lee, & Yianneskis, 2003). The flow in these devices is known to be complex – having a wide range of temporal and spatial scales – especially in the case of the turbulent regime. In recent years, and as in other turbulent flow problems, there has been an increasing interest in the study of organised flow motions or coherent structures, as a complement to the traditional approach of investigating long-term turbulence statistics.

Coherent structures are regions of space and time (significantly larger than the smallest turbulence scales) within which the flow field has a characteristic coherent pattern (Pope, 2000). Typically, efforts to isolate coherent structures follow two basic lines of approach (Cantwell, 1981): (i) identification of instantaneous flow structures and (ii) construction of stochastic representations. Approach (i) consists of using various methods to identify discernible flow patterns, e.g. direct flow visualisation, or the isolation of connected regions in the flow where a relevant property (vorticity, for example) is more intense. On the other hand, approach (ii) consists of implementing an eduction technique to obtain representations of the most probable states of the flow according to an applied criterion. A well-known example of approach (ii) is proper orthogonal decomposition (POD).

The POD procedure is also known as Karhunen–Loève expansion or principal components analysis (Sirovich, 1987). In the context of turbulent flows, POD was introduced by Lumley (1967), and was applied for the first time in the study of wall-bounded turbulence (Bakewell & Lumley, 1967). The basic idea behind POD is not complicated. For an ensemble of realisations, one is looking for a set of orthonormal basis vectors which, on average, are the 'most similar' (Berkooz, Holmes, & Lumley, 1993) to all members of the ensemble. Such empirical bases are often denoted as POD modes. Subsequently, once the POD modes are found, each realisation may be represented by a (linear) superposition of the deterministic modes modulated by corresponding random, uncorrelated, coefficients. Furthermore, it can be shown – see Holmes, Lumley, Berkooz, and Rowley (2012) – that a truncated expansion in terms of ordered POD modes gives a representation that is better than any other linear representation, having the same number of modes, in terms of capturing the energy content. That is, the representation is optimal even with just a few POD modes and not only in an asymptotic sense. In consequence, when considering the POD representation of the velocity field, it is not surprising that some researchers denote the POD modes as characteristic eddies (Lumley, 1970).

During the last two decades or so, the POD procedure has been implemented for the study of stirred tanks in transitional (see e.g. Charalambidou, Micheletti, & Ducci, 2023; Fan et al., 2022; Hasal, Montes, Boisson, & Fořt, 2000; Raju, Balachandar, Hill, & Adrian, 2005) and turbulent (see e.g. de Lamotte, Delafosse, Calvo, & Toye, 2018; Doulgerakis, Yianneskis, & Ducci, 2011; Hasal et al., 2000; Moreau & Liné, 2006; Raju et al., 2005) flow regimes. Nevertheless, previous works considered two-dimensional velocity fields and it was not until recently that POD analyses and reconstructions based on three-dimensional (3-D) velocity fields have been reported. Janiga (2019) and Mikhaylov, Rigopoulos, and Papadakis (2021, 2023a, 2023b) considered simulations of unbaffled stirred tanks. Janiga (2019) performed large-eddy simulation (LES) of the turbulent regime where the flow is agitated with a pitched-blade turbine with three blades. The movement of the propeller was incorporated using the sliding mesh approach (Murthy, Mathur, & Choudhury, 1994), and the POD analysis was performed in two different regions of the tank (a per-zone approach). A fixed region was considered to analyse macrostabilities (large-scale, long-lived, quasi-periodic structures; see e.g. Nikiforaki et al., 2003), whereas a rotating region was examined to explore the structures related to the periodic passage of the blades, i.e. trailing vortices (counterrotating vortex pairs generated behind the upper and lower edges of each impeller blade; see e.g. Escudié, Bouyer, & Liné, 2004; Van't Riet & Smith, 1975). On the other hand, Mikhaylov et al. (2021) and Mikhaylov et al. (2023a) performed direct numerical simulations of transitional flow where the rotational motion is induced by a six-blade Rushton turbine. The movement of the impeller was addressed through the frozen motor approach (Luo, Issa, & Gosman, 1994) and the POD technique targeted the reconstruction of trailing vortices based on velocity (Mikhaylov et al., 2021) and pressure

https://doi.org/10.1017/flo.2023.26 Published online by Cambridge University Press

(Mikhaylov et al., 2023a) data from a small number of probing points. After these two works, for the same tank geometry and stirrer, Mikhaylov et al. (2023b) performed LES of turbulent flow with the aim of studying and reconstructing macrostabilities from sparse measurements. Interestingly, in this study, the first pair of modes are associated with trailing vortices that appear to form a macrostability as they propagate away from the blades, whilst the second pair of modes are believed to represent the precession of large structures around the impeller shaft. Conversely, there is a single study about POD applied to 3-D velocity fields in baffled stirred tanks. Mayorga, Morchain, and Liné (2022) considered the turbulent flow in a four-baffled stirred tank operating with a Rushton turbine. In Mayorga et al. (2022), the turbulent flow is modelled with an unsteady Reynolds-averaged Navier–Stokes method and, as in Janiga (2019), a sliding mesh approach is used for the propeller. Yet, on the contrary, a global approach is proposed for the POD reconstruction of mean and organised flow motion, the latter due to the periodic passages of the blades in the stirred tank.

Considering the works mentioned previously (Janiga, 2019; Mayorga et al., 2022; Mikhaylov et al., 2021, 2023a, 2023b), it is noticeable that the attention given to POD modes other than those related to the mean flow motion, trailing vortices and macroinstabilities has been minor. In a complex flow, the attractiveness of the POD technique resides in its capability for yielding an optimal (linear) stochastic representation of a velocity signal in the sense of capturing, on average, the largest amount of kinetic energy (KE). Therefore, energetic modes associated with turbulent fluctuations and their resulting velocity reconstructions are certainly also worth exploring. Of course, information about the mean flow pattern, trailing vortices and macroinstabilities is still of utmost importance. The mixing efficiency, as well as product quality, are influenced by the flow patterns occurring in the stirred vessel (Chhabra & Richardson, 2008). Power consumption – perhaps the most important parameter from a practical point of view – is majorly affected by the mean flow (Mikhaylov et al., 2023a). In addition, the disruption of trailing vortices also impacts the power consumption by affecting the time-average recirculation pattern on the suction side and leading to a decrease in energy dissipation (Başbuğ, Papadakis, & Vassilicos, 2018a). Mixing time is affected as well by the disruption of the trailing vortices – due to the changes in the mean flow circulation inside the vessel (Başbuğ, Vassilicos, & Papadakis, 2018b) – and by macroinstabilities, when their cores are used for feed insertion (Ducci & Yianneskis, 2007). Furthermore, trailing vortices are also known to provide a source of turbulence (Escudié et al., 2004) and to produce regions of high strain in their proximity (Bouremel, Yianneskis, & Ducci, 2009) where mixing could be performed more efficiently.

Keeping in mind Hussain & Reynolds's (1970) triple decomposition, the goal of the present paper is to investigate, for a baffled stirred tank and two different fluids, the most energetic POD modes corresponding to mean, organised (periodic) and turbulent motion. Regarding the latter, the idea is to use the higher-order modes to also reconstruct 3-D velocity fields mostly representing the turbulent fluctuations. These approximations to the velocity fluctuations may then be used to explore turbulent structures in the agitated vessel. More specifically, vortical structures are considered and their shape is studied. In the context of stirred tanks, vortices are extremely important due to their role in mixing and possibly in the breakup and coalescence of fluid particles (drops and bubbles) in turbulent dispersions. Indeed, one plausible scenario is that topological changes experienced by the fluid particles are strongly dependent upon the interactions with surrounding swirling-like structures. For instance, a drop embedded into a structure much larger than it may be advected with the structure with little deformation, whilst if the structure is of a comparable size and strong enough to overcome the cohesive forces will cause its breakage into two or more daughter particles. Moreover, not only are the size, intensity and proximity to the fluid particles likely deciding factors but also the shape, number of structures and type of interactions. A droplet squeezed between two corotating structures could be torn apart whereas between two counterrotating ones could be just elongated (Kresta & Brodkey, 2004). Here, the shape of the structures is crucial since it determines the amount of contact area and how different properties are distributed which, in turn, affects important integral quantities such as circulation (macroscopic measure of rotation). In fact, many phenomenological models for the breakup and coalescence processes (see e.g. Liao and Lucas (2009, 2010) and Solsvik, Tangen, and Jakobsen (2013) for reviews of these models)

https://doi.org/10.1017/flo.2023.26 Published online by Cambridge University Press

are based on several simplifications to these factors, including the interaction of fluid particles with structures having matching size and being of spherical shape. In this work, our aim is to address as well how reasonable this last-mentioned assumption is for vortices arising due to the most energetic, POD-reconstructed, velocity fluctuations.

The paper is organised as follows. Section 2 outlines the numerical experiments and the database considered for the analyses. Section 3 summarises the POD procedure and the 'method of snapshots' (Sirovich, 1987), which is an alternative and (in general) less computationally expensive method. Section 3 describes as well an objective version of the traditional Q-criterion (Hunt, Wray, & Moin, 1988) considered to identify vortical structures. Material objectivity (frame invariance) is a highly desirable property for vortex criteria (Günther, Gross, & Theisel, 2017), especially in case of rotating flows (see Günther, Schulze, & Theisel, 2016). Next, § 4 presents the modal analysis and the characterisation of the identified vortical structures in terms of their shape. Finally, § 5 provides some concluding remarks.

2. Numerical experiments

To perform POD, a database obtained from LES of an 11 l, baffled stirred tank with a Rushton-type impeller is considered. The simulations were performed using the commercial package Ansys FLUENT (version 19.1, Ansys Inc., Canonsburg, PA). The minimum and maximum grid sizes were set to 2×10^{-4} and 4×10^{-3} m, respectively. Such resolution was deemed adequate for the LES considering that rough estimates – based on isotropic conditions, volume-averaged dissipation rate and turbulent KE – for the Taylor microscale and the Kolmogorov length scale (see e.g. Escudié & Liné, 2003; Sharp & Adrian, 2001) were mostly within the order of 10^{-4}–10^{-3} m and of the order of 10^{-5} m, respectively. These estimates are for the Newtonian case which is the most restrictive (see next paragraph). The computations were initialised with the results obtained from steady Reynolds-averaged Navier–Stokes simulations, and the volume-averaged torque and turbulent KE were monitored during the LES. Instantaneous realisations (samples) were only taken after reaching statistically stationary conditions.

For the analyses, two test cases are considered. The stirred vessel operates at 800 rpm (impeller frequency $f_N \approx 13.33$ r.p.s. or Hz), and the working fluid is either water (Newtonian) or a 0.2 wt% carboxymethyl cellulose (CMC) solution presenting shear-thinning behaviour (see e.g. Irgens, 2014). Information about the tank configuration is given in figure 1 and table 1. A summary of other relevant parameters is presented in table 2. Note that the normalised total sampling time reported in table 2 corresponds to approximately 22.67 cycles of the stirrer. On the other hand, the reported normalised time between collected samples corresponds to a normalised sampling frequency, f_{sam}/f_N, of approximately 18.75. Such f_{sam} is suitable for the study of flow structures of intermediate scale taking place close to and at the blade passage frequency, $f_{BPF} = 6f_N$ (six times the impeller frequency for a six-bladed disc turbine). Moreover, the total sampling time is also large enough to capture many cycles of these structures and, potentially, even traces of other quasi-periodic, long-lived structures, i.e. macroinstabilities.

For further details about the LES and the test cases, see Arosemena et al. (2022).

3. Methods

3.1. The POD procedure and the method of snapshots

The classical POD procedure aims to find a set of optimal basis vectors to represent the flow field data, e.g. $\boldsymbol{U} \in \mathbb{R}^{n\times m}$, where $\boldsymbol{U}$ denotes a data matrix comprised of instantaneous velocity fields $\boldsymbol{u}$, n is the number of grid points times the number of variables (three in the case of a 3-D velocity field) and m is the number of collected realisations. In other words, one has an extremisation problem resulting in the following eigenvalue formulation (Holmes et al., 2012):

$$\boldsymbol{R}\boldsymbol{\phi}_{(k)} = \lambda_{(k)}\boldsymbol{\phi}_{(k)}, \quad \boldsymbol{\phi}_{(k)} \in \mathbb{R}^{n\times 1}, \quad \lambda_{(1)} \geq \cdots \geq \lambda_{(n)} \geq 0, \quad k = 1, \ldots, n, \tag{3.1}$$

https://doi.org/10.1017/flo.2023.26 Published online by Cambridge University Press

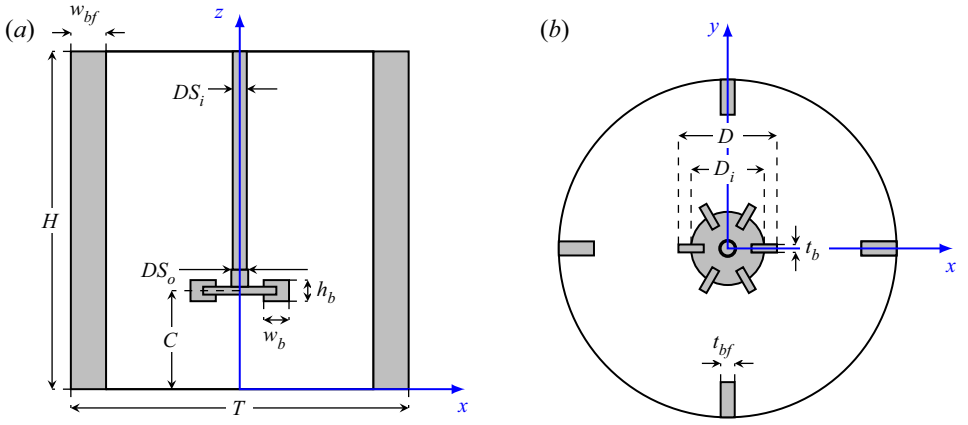

Figure 1. *Geometrical configuration of the stirred tank considered in the LES: (a) cross-sectional view and (b) top view. The values of the geometrical parameters are given in table 1. The Cartesian coordinate system is shown in blue. Figure adapted from Arosemena et al. (2022), copyright 2022 AIP Publishing.*

Table 1. *Geometrical details for the stirred tank considered in the LES. The tank diameter $T = 24$ cm. For corresponding schematic representation, see figure 1.*

Parameter	Value
H/T	1.000
C/T	0.292
D/T	0.292
D_i/T	0.217
h_b/T	0.063
t_b/T	0.008
w_b/T	0.075
DS_i/T	0.042
DS_o/T	0.050
t_{bf}/T	0.042
w_{bf}/T	0.104

Table 2. *Parameters of the LES. Here W800/C800 refers to simulation case with water/0.2 wt% CMC where the tank operates at 800 r.p.m. Time t_A denotes the total sampling time (after discarding the initial transients), u_{tip} is the tip speed of the impeller and Δt is the time between the samples. Parameter Re_{mix} is a mixing Reynolds number based on the working fluid density ρ, the impeller rotational speed N and diameter D, and an apparent fluid viscosity μ_a for an average strain rate according to the Metzner–Otto correlation for a Rushton-type stirrer (see Metzner & Otto, 1957). For water, μ_a is the dynamic viscosity whereas for the 0.2 wt% CMC case, μ_a is computed according to the Carreau fluid model (see Arosemena et al. (2022) for further details).*

Parameter	W800/C800
$t_A/(T/u_{tip})$	20.769
$\Delta t/(T/u_{tip})$	48.900×10^{-3}
$Re_{mix} = \rho N D^2/\mu_a$	$65.333/1.616 \times 10^3$

https://doi.org/10.1017/flo.2023.26 Published online by Cambridge University Press

where $\boldsymbol{R} = \boldsymbol{U}\boldsymbol{U}^{\boldsymbol{T}}\boldsymbol{W}/m \in \mathbb{R}^{n\times n}$ is the weighted covariance matrix, $\boldsymbol{\phi}_{(k)}$ is the set of eigenvectors or POD modes and $\lambda_{(k)}$ are the corresponding eigenvalues. Note that $\boldsymbol{W}$ is an $n \times n$ matrix arising after considering the discrete form of the inner product (see e.g. Smith, Moehlis, & Holmes, 2005; Taira et al., 2017) and which accounts for the grid non-uniformity. The optimal linear expansion is then given by

$$\boldsymbol{U} = \sum_{k=1}^{n} \boldsymbol{\phi}_{(k)}\boldsymbol{a}_{(k)} \approx \sum_{k=1}^{r} \boldsymbol{\phi}_{(k)}\boldsymbol{a}_{(k)}, \quad \boldsymbol{a}_{(k)} \in \mathbb{R}^{1\times m}, \quad r < n, \tag{3.2}$$

where the set of uncorrelated temporal coefficients $\boldsymbol{a}_{(k)}$ is found by projecting the input data into the k-mode. Usually, a satisfactory upper bound r for the truncated series is much less than the total number of modes n.

An issue with the classical POD method is that for a very large n, solving the eigenvalue problem becomes impractical and sometimes even not possible. An alternative approach is the method of snapshots proposed by Sirovich (1987). The basic idea is that instead of having a decomposition involving deterministic spatial modes and random time coefficients, one may have a decomposition in terms of deterministic temporal modes with random spatial coefficients (Weiss, 2019). This is computationally advantageous since, typically, $m << n$ and the resulting eigenvalue problem involves a matrix of size $m \times m$ rather than of size $n \times n$. Of course, the method does not provide a full POD representation, and to be successful the chosen realisations must be representative of the flow statistics (Jiménez, 2018). In any case, once the reduced eigenvalue problem is solved, one can recover the leading spatial POD modes through a transformation as shown next.

In the method of snapshots, the resulting eigenvalue problem is as follows (Holmes et al., 2012):

$$\hat{\boldsymbol{R}}\hat{\boldsymbol{\phi}}_{(k)} = \lambda_{(k)}\hat{\boldsymbol{\phi}}_{(k)}, \quad \hat{\boldsymbol{\phi}}_{(k)} \in \mathbb{R}^{m\times 1}, \quad \lambda_{(1)} \geq \cdots \geq \lambda_{(m)} \geq 0, \quad k = 1, \ldots, m, \tag{3.3}$$

where $\hat{\boldsymbol{R}} = \boldsymbol{U}^{\boldsymbol{T}}\boldsymbol{W}\boldsymbol{U}/m \in \mathbb{R}^{m\times m}$ is the reduced matrix, sharing the same leading eigenvalues with $\boldsymbol{R}$ (Taira et al., 2017), and $\hat{\boldsymbol{\phi}}_{(k)}$ is the temporal eigenvector. Thereafter, the spatial modes are recovered from

$$\boldsymbol{\phi}_{(k)} = \boldsymbol{U}\hat{\boldsymbol{\phi}}_{(k)} \frac{1}{m^{1/2}\lambda_{(k)}^{1/2}} \in \mathbb{R}^{n\times 1}, \quad k = 1, \ldots, m, \tag{3.4}$$

which is obtained by considering the singular value decomposition (see e.g. Press, Teukolsky, Vetterling, & Flannery, 2007) of $\boldsymbol{W}^{1/2}\boldsymbol{U}/m^{1/2}$.

3.2. An objective version of the Q-criterion

Swirling-like structures or vortices are the 'sinews and muscles of fluid motion' (Küchemann, 1965). This is even more so when the flow is turbulent and/or rotational. Over the years, many vortex identification methods have been proposed (see Epps (2017) for a recent review). The Q-criterion (Hunt et al., 1988) is among the most popular ones. In this method, a vortex is a local region in which there is an excess of rotation rate relative to the strain rate (Chakraborty, Balachandar, & Adrian, 2005). Nevertheless, the Q-criterion, as other Galilean-invariant methods such as the Δ-criterion (Chong, Perry, & Cantwell, 1990) or the λ_2-criterion (Jeong & Hussain, 1995), has an important shortcoming: it is not objective. That is, rotational invariance, an essential feature for rotating flows, it is not fulfilled (see Haller, 2005). In this respect, Haller (2021) remarked that these local vortex criteria may effectively be objectivised by replacing the spin/rotation rate tensor by a spin-deviation tensor. The spin-deviation tensor is defined as the difference between the original rotation rate tensor and its instantaneous spatial average (see Haller, Hadjighasem, Farazmand, & Huhn, 2016). This procedure was proposed and implemented by Liu, Gao, and Liu (2019a) and Liu, Gao, Wang, and Liu (2019b) to objectivise the Rortex criterion (Liu, Gao, Tian, & Dong, 2018; Tian, Gao, Dong, & Liu, 2018) and the omega method

https://doi.org/10.1017/flo.2023.26 Published online by Cambridge University Press

(Liu, Wang, Yang, & Duan, 2016). The same procedure has also been implemented by Arosemena et al. (2022) to objectivise the Q-criterion, and it may be summarised as follows.

First, the spin-deviation tensor is computed as

$$\boldsymbol{\Omega}_\star = \boldsymbol{\Omega} - \langle \boldsymbol{\Omega} \rangle \,, \tag{3.5}$$

where $\boldsymbol{\Omega} = \frac{1}{2}[\boldsymbol{\nabla u} - (\boldsymbol{\nabla u})^{\mathrm{T}}]$ is the spin/rotation rate tensor and $\langle \boldsymbol{\Omega} \rangle (t) = (1/\mathcal{V}) \int_{\mathcal{V}} \boldsymbol{\Omega} \, \mathrm{d}\mathcal{V}$ is the instantaneous spatial average of $\boldsymbol{\Omega}$ over the full flow domain $\mathcal{V}$.

Next, the Q-criterion is reformulated as

$$Q_\star = \tfrac{1}{2} \left[|\boldsymbol{\Omega}_\star|^2 - |\boldsymbol{S}|^2 \right], \tag{3.6}$$

which is objective (not observer-dependent). Here $\boldsymbol{S} = \frac{1}{2}[\boldsymbol{\nabla u} + (\boldsymbol{\nabla u})^{\mathrm{T}}]$ is the strain rate tensor.

4. Results

Before discussing the results, it is important to clarify some points about the input data. The impeller movement in the LES is implemented by means of the sliding mesh approach. Therefore, regardless of having an inertial or a rotational frame of reference, part of the mesh is moving as the simulations proceed. In such cases, to date, the following strategies have been implemented: (i) the POD method is applied in a per-zone manner where different modes and coefficients are found for the stationary and rotating domains or zones (Janiga, 2019) and (ii) the POD method is applied in a global manner considering the two zones altogether (Mayorga et al., 2022). Both strategies are feasible for POD reconstruction of the velocity field yet pose some issues for the analysis of the modes. In the case of the per-zone treatment, the connection between modes in the two zones and their energy content is rather ambiguous. On the other hand, with respect to the global treatment, direct physical interpretation of the POD modes is not possible since the modes are referenced to the elements of the mesh (cells), the positions of which change from time step to time step in the rotating zone.

In this work, instead, the flow-field data are interpolated to a fixed set of points through Sibson (natural neighbour) interpolation (Sibson, 1981). This interpolation scheme is more computationally expensive than others; however, it is known to work well with scattered data (Park, Linsen, Kreylos, Owens, & Hamann, 2006). The query points are set to those of the mesh of the first saved snapshot for the cases outlined in table 2. Here, as with any interpolation method, the issue is how well the interpolated data approximate the original values and may reflect the actual physical process. Appendix A presents a comparison between a randomly selected velocity field for case W800 and its natural neighbour interpolation.

4.1. The POD modal analysis

The amount of KE contributed by each POD mode is found in the corresponding eigenvalue. Figure 2(*a*) displays the energy contained in the k-mode normalised by the energy contained in all modes. Mode 1 contains most of the total energy (≈60 %–70 %) followed by modes 2 and 3 with very similar energy levels (≈5 %). In comparison, the amount of energy in the remaining modes is fairly small (less than 1% for $k > 6$). From figure 2(*a*) one can also observe that the decay of energy is slow, especially as the theoretical estimate for the inertial subrange (Knight & Sirovich, 1990) is approached. Moreover and as expected, this behaviour is more prominent for the higher-Reynolds-number case, i.e. W800. This is more clearly seen in figure 2(*b*) where the cumulative percentage of total KE is shown. It is also worth noting that at least 95 % of the total KE is captured once about a third of the total number of modes m is considered. Lastly, regarding the sensitivity of the results to the number of considered snapshots, Appendix B compares the fraction of total KE for case W800 – presented in figure 2(*a*) – with the fraction when the number of snapshots is doubled.

https://doi.org/10.1017/flo.2023.26 Published online by Cambridge University Press

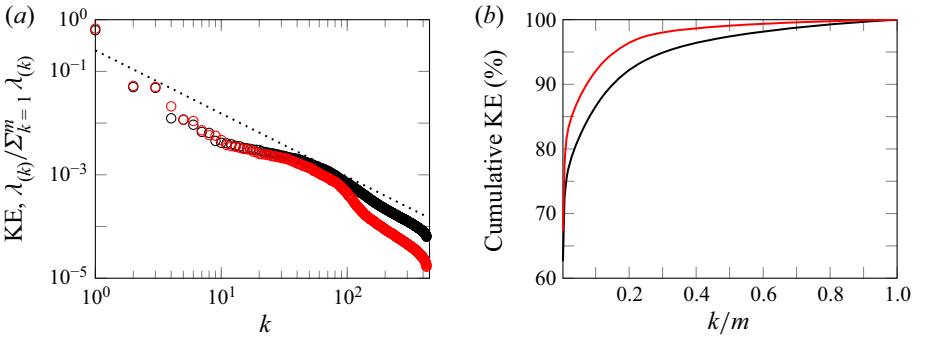

Figure 2. *The KE content in POD modes: (a) fraction of total KE versus mode number k and (b) percentage cumulative amount of KE versus k/m. Total number of modes, m = 426. Colours black and red correspond to cases W800 and C800, respectively. See table 2. In (a), the dotted line represents the −11/9 power law (Knight & Sirovich, 1990).*

In the following, the most energetic modes and their corresponding temporal coefficients are discussed.

Mode 1

Mode 1 (denoted as the zeroth mode by some researchers) is probably representing the mean flow. This is a classical result when POD is applied to the instantaneous velocity fields (Moreau & Liné, 2006). Figure 3 depicts the first eigenvector at selected planes for cases W800 and C800. Figure 3(*a*,*b*) shows the y, z components at $x/T = 0$, a cross-section between two baffles, whilst figure 3(*c*,*d*) shows the x, y components at $z/T \approx 0.4$, a horizontal plane above the impeller. From figure 3(*a*,*b*), one can see the impeller stream and the lower and upper circulation loops. On the other hand, from figure 3(*c*,*d*), one can discern the expected effect of using vertical baffles; no gross vortexing is taking place and counterrotating structures – with respect to the rotating direction of the impeller – are appearing behind the baffles. All these patterns are typical of the mean flow for the configuration considered (see e.g Chhabra & Richardson, 2008). Furthermore, as reported in previous studies (see e.g. de Lamotte et al., 2018), the temporal coefficient for mode 1 is seemly a constant which is being superimposed by small-amplitude, higher-frequency signals. See temporal signal in figure 4(*a*), displayed only for $t/(T/u_{tip}) \in [0, 1]$, and the corresponding power spectral density (PSD) in figure 4(*b*). As seen from the PSD, aside from the main peak at $f/f_N = 0$, there are two other, less noticeable, peaks: one at f_{BPF} and another at its nearest overtone. Note that the latter is being masked due to the considered sampling frequency: $|2f_{BPF} - (\mathcal{N}f_{sam})|/f_N \approx 6.75$, where $(\mathcal{N}f_{sam})$ is the integer multiple of f_{sam} closest to the frequency of interest, $2f_{BPF}$.

It is also interesting to note that there are some differences in the first POD mode of two fluid cases. Compared with the Newtonian fluid case, there are more quasi-stagnant regions, an overall attenuation of the circulation loops and the structures behind the baffles and more asymmetry below the impeller for the shear-thinning fluid. These factors suggest poorer macromixing for case C800, especially in regions away from the impeller.

Modes 2 and 3

Modes 2 and 3 are probably coupled – as mentioned previously in this section, these modes have nearly identical energy content – and represent organised motion due to the periodic passage of the blades, namely trailing vortices as reported in previous works (see e.g. Gabelle, Morchain, & Liné, 2017; Liné, Gabelle, Morchain, Anne-Archard, & Augier, 2013). Figure 5(*a–d*) shows the y, z components of the second and third eigenvectors at $x/T = 0$ for cases W800 and C800. As can be seen and as expected in the case of trailing vortices, modes 2 and 3 reveal swirling-like, counterrotating patterns exhibiting

https://doi.org/10.1017/flo.2023.26 Published online by Cambridge University Press

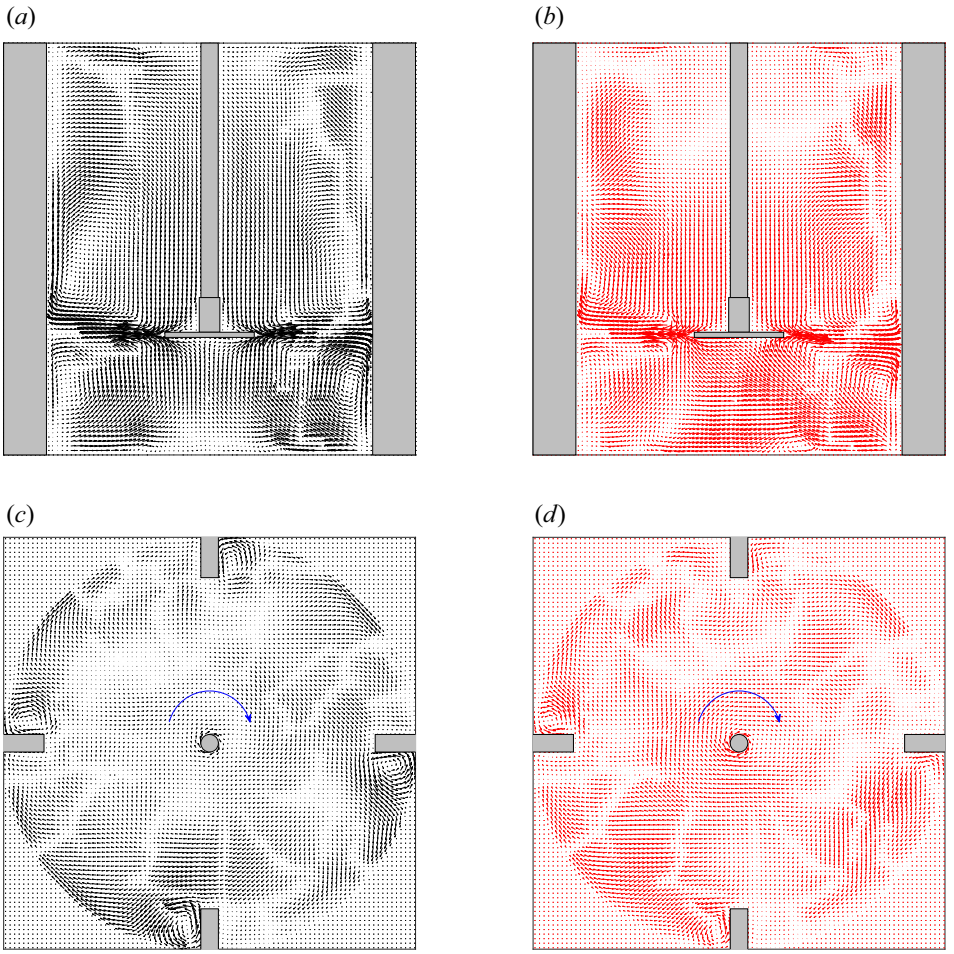

Figure 3. *Visualisation of POD mode 1 in (a,b) a vertical plane between two baffles at $x/T = 0$ and (c,d) a horizontal plane above the impeller at $z/T \approx 0.4$. In (c,d), the blue arrow indicates the rotating direction of the stirred vessel. Colours black and red correspond to cases W800 and C800, respectively. See table 2.*

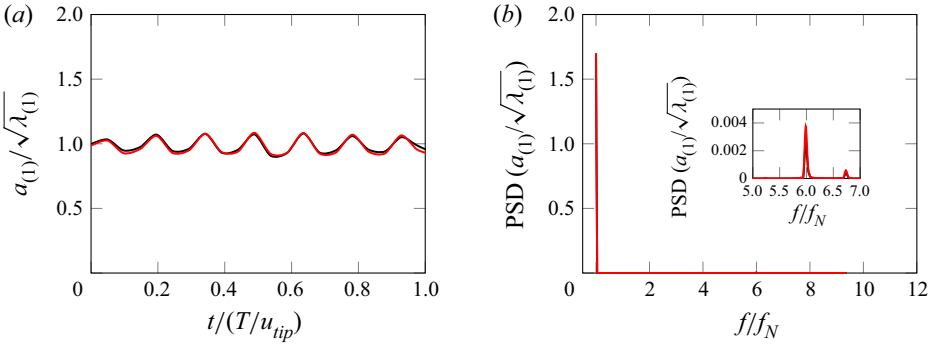

Figure 4. *Temporal coefficient of POD mode 1: (a) normalised temporal coefficient and (b) PSD corresponding to the normalised coefficient. Here, f_N represents the impeller frequency in revolutions per second. Colours black and red correspond to cases W800 and C800, respectively. See table 2.*

https://doi.org/10.1017/flo.2023.26 Published online by Cambridge University Press

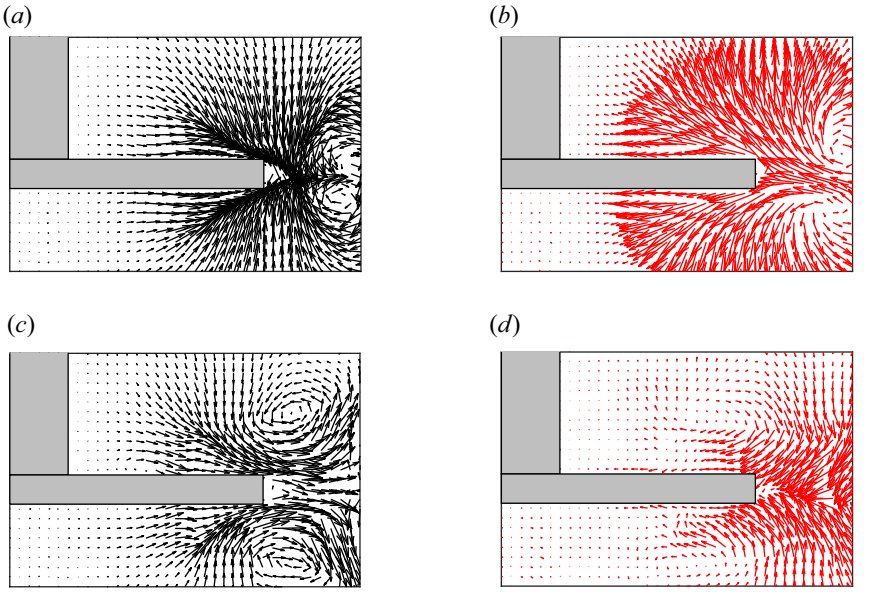

Figure 5. *Visualisation of POD modes 2 and 3 in a vertical plane between two baffles at $x/T = 0$ and in the vicinity of the impeller: (a,b) mode 2 and (c,d) mode 3. Colours black and red correspond to cases W800 and C800, respectively. See table 2.*

symmetry with respect to the plane of the impeller ($z = C$), albeit these are not as pronounced for the shear-thinning fluid case when compared with the Newtonian case. In addition, the analysis of the temporal coefficients corresponding to modes 2 and 3 evidences their coupled periodic nature. Figure 6(*a*), presenting the normalised temporal coefficients for $t/(T/u_{tip}) \in [0, 1]$, allows one to note an apparent out-of-phase, sinusoidal-like behaviour in the signals. Moreover, as displayed in figure 6(*b*), their corresponding PSDs are peaking at the blade passage frequency which emphasises the connection between modes 2 and 3 and the periodic motion due to the passages of the blades. Here, note as well there is a second, barely noticeable, peak at $f/f_N \approx 6.75$. As commented before while discussing the temporal coefficient for POD mode 1, this peak happens at the nearest overtone of f_{BPF} with aliasing due to the considered f_{sam} and corresponds to a superimposed, small-amplitude, signal.

Another tool to highlight the harmonic coupling between the modes is the cross-plotting of their temporal coefficients (van Oudheusden, Scarano, van Hinsberg, & Watt, 2005). This is done in figure 6(*c*) and as can be seen, although the coefficients are statistically uncorrelated, they are not independent and instead are scattered around an ellipse. This is typical of sinusoidal signals out of phase.

Modes 4 to 11

The POD modes 4 to 11 are probably representing either complex harmonic motion linked to the trailing vortices, or a macroinstability. Previous investigations of stirred tanks have shown that modes following modes 2 and 3 may also exhibit counterrotating structures that are almost symmetric with respect to $z = C$ (see e.g. Gabelle et al., 2017; Liné et al., 2013). Moreover, together with modes 2 and 3, these structures depict a convective pattern resembling the vortex shedding behind bluff bodies reported in many works (Liné et al., 2013). Meanwhile, depending on the total sampling time (here t_A; see table 2), it is possible that the modes following modes 2 and 3 are representing a macroinstability (see e.g. Doulgerakis, Yianneskis, & Ducci, 2009).

In the following and to shorten the discussion, the visualisation of all these POD modes (4 to 11) is not shown nor the time evolution of their corresponding coefficients. Instead, here the phase portrait of the coefficients of these modes with $a_{(3)}$ are investigated to also gain insight into the modes. In the

https://doi.org/10.1017/flo.2023.26 Published online by Cambridge University Press

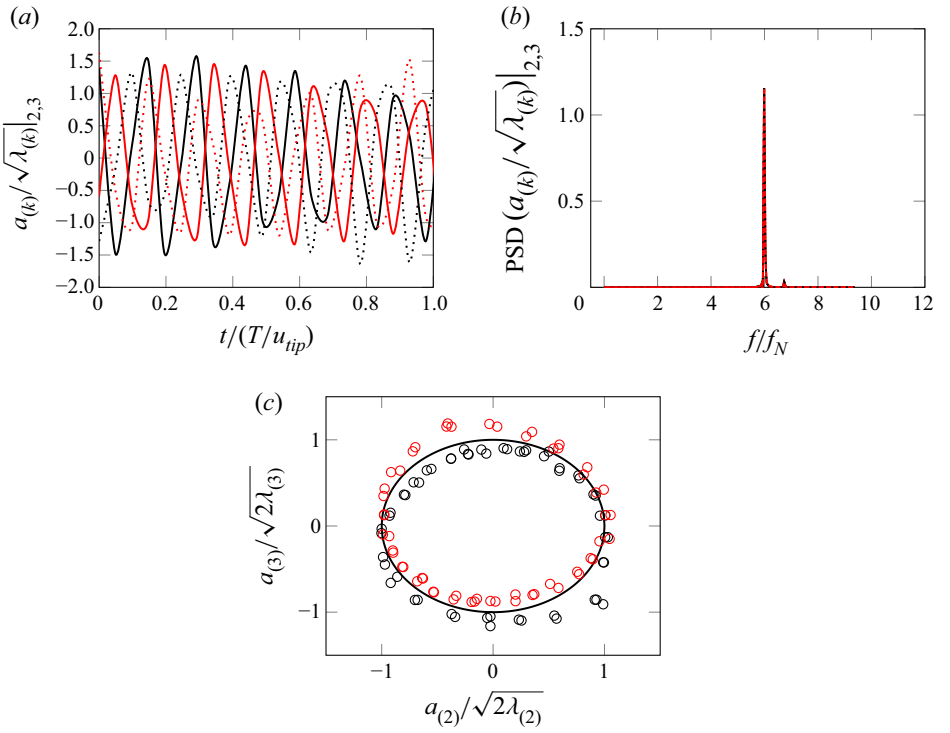

Figure 6. *Temporal coefficients of POD modes 2 and 3: (a) normalised temporal coefficients, (b) PSD corresponding to the normalised coefficients and (c) phase portrait of the normalised coefficients. In (a,b), continuous and dotted line styles are used for normalised $a_{(2)}$ and $a_{(3)}$, respectively. In (c), the continuous line represents the unitary ellipse, and to avoid excessive clustering not all data points are displayed. Here, f_N represents the impeller frequency in revolutions per second. Colours black and red correspond to cases W800 and C800, respectively. See table 2.*

case of periodic vortex shedding, $a_{(3)}$ would be one of the basic harmonics. From figures 7(*a*)–(*h*), it is clear that there is some relation between $a_{(3)}$ and the coefficients corresponding to modes 4, 5, 7, 8 and 9 in case W800 and those corresponding to modes 5, 6, 8 and 9 in case C800. The displayed patterns are similar to Lissajous curves which, indeed, suggests complex harmonic behaviour. At this point, it is worth mentioning that (in general) the POD technique is not suitable for isolating structural coherence based on observations about the temporal coefficients, since a given modulated POD mode may encompass different signals and physical phenomena. Therefore, other statistical techniques such as dynamic mode decomposition (see Schmid, 2010) are preferred when one is interested in the 'best fit' for approximating the dynamics of the data. Nevertheless, for periodic and convective phenomena (as in the case of vortex shedding), it is known that both linear decompositions (POD and dynamic mode decomposition) yield remarkably similar structures (Schmid, Violato, & Scarano, 2012).

On the other hand, regarding the remaining temporal coefficients – $a_{(6)}, a_{(10)}$ and $a_{(11)}$ for W800, and $a_{(4)}, a_{(7)}, a_{(10)}$ and $a_{(11)}$ for C800 – there is no distinctive relation between them and $a_{(3)}$. Besides, when considering the time evolution of these coefficients, an exceedingly long signal is uncovered (see figure 8*a*,*b*). Macroinstabilties are large temporal and spatial fluctuations of the flow (Galletti, Paglianti, & Yianneskis, 2005) arising due to two distinct mechanisms: (i) precessional vortex motion around the shaft (see e.g. Nikiforaki et al., 2003) and (ii) the impingement of the jet-like discharge stream on the vessel boundaries (see e.g. Roussinova, Kresta, & Weetman, 2003). In the turbulent flow regime, the precessional macroinstabilities result in a characteristic frequency which is smaller than the characteristic

https://doi.org/10.1017/flo.2023.26 Published online by Cambridge University Press

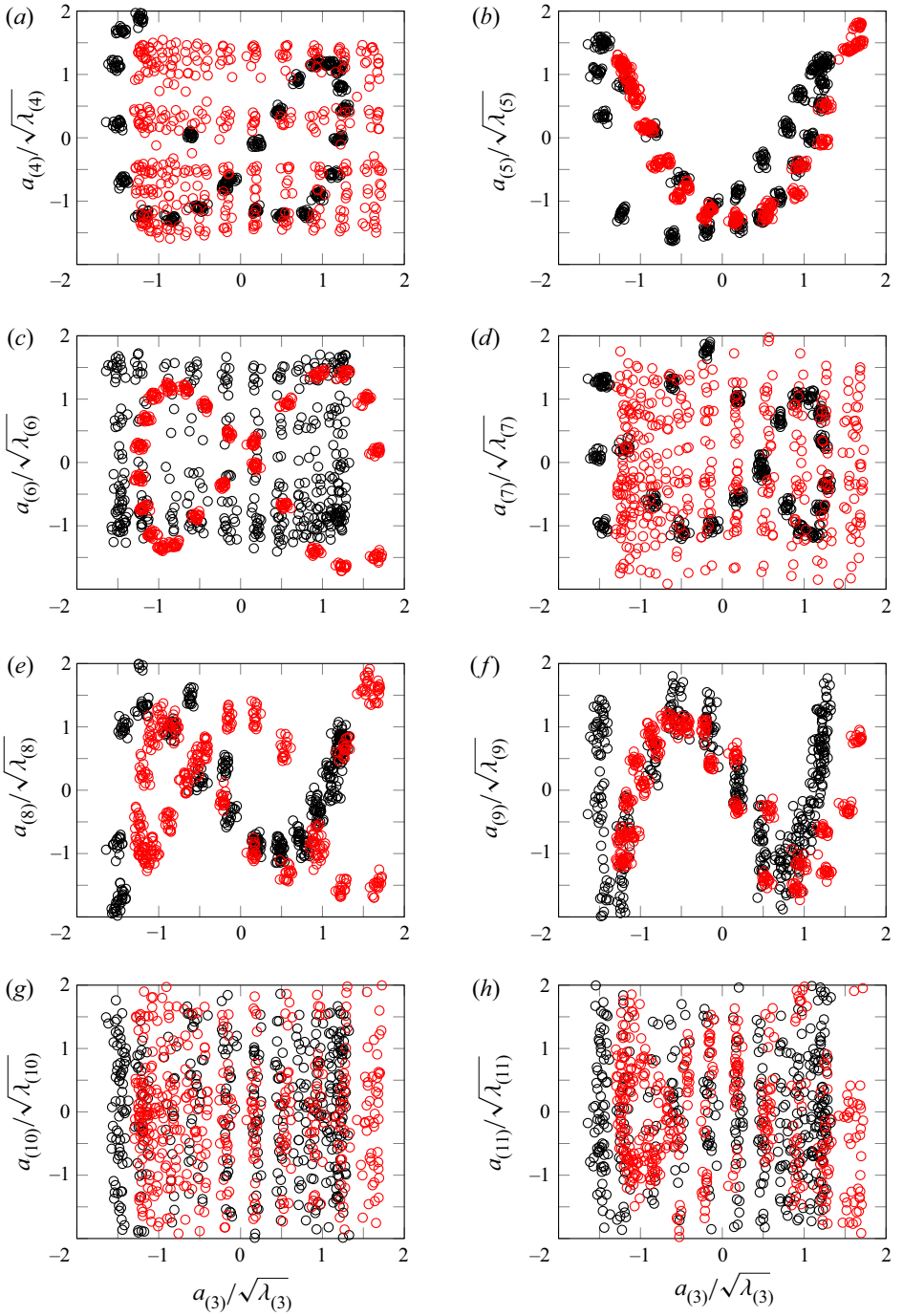

Figure 7. *Phase portrait of normalised coefficients, series of mode 3 and (a) mode 4 coefficients, (b) mode 5 coefficients, (c) mode 6 coefficients, (d) mode 7 coefficients, (e) mode 8 coefficients, (f) mode 9 coefficients, (g) mode 10 coefficients and (h) mode 11 coefficients. Colours black and red correspond to cases W800 and C800, respectively. See table 2.*

https://doi.org/10.1017/flo.2023.26 Published online by Cambridge University Press

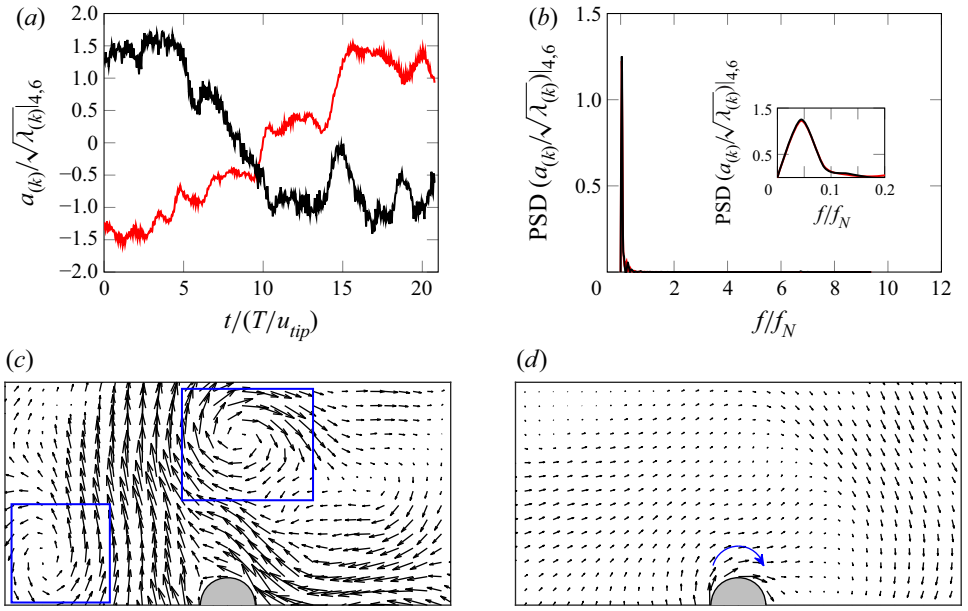

Figure 8. *Traces about precessional macroinstabilities, POD mode 6 for W800 and POD mode 4 for C800: (a) normalised temporal coefficients, (b) PSD corresponding to the normalised coefficients, (c) visualisation of mode 6 at $z/T \approx 0.4$ and (d) visualisation mode 1 at $z/T \approx 0.4$. In (c), the blue boxes mark regions with precessional patterns. In (d), the blue arrow indicates the rotating direction of the stirred vessel. Here, f_N represents the impeller frequency in revolutions per second. Colours black and red correspond to cases W800 and C800, respectively. See table 2.*

frequency of the jet-impingement macroinstabilities by an order of magnitude. The frequency of the precessional macroinstabilities is also smaller than the characteristic frequency for trailing vortices by two orders of magnitude (Doulgerakis et al., 2009). In consequence, the behaviour for the remaining temporal coefficients is likely reflecting the presence of precessional macroinstabilities in the flow. Figure 8(*c*,*d*) displays the *x*, *y* components of the sixth and first eigenvectors at $z/T \approx 0.4$ for case W800, respectively. The former shows precessional patterns around the shaft (see blue boxes in figure 8*c*).

Lastly, it is important to stress the limitation of our data in terms of characterising precessional macroinstabilities. For the proper study of these periodic or quasi-periodic motions, one requires the recording of at least some full cycles to minimise statistical errors. For example, Ducci and Yianneskis (2007) considered four sets of data corresponding to the same experiment where, for each set, a complete cycle was recorded. Additionally, and with the purpose of capturing at least one full cycle of the precessional motion, the temporal behaviour of $a_{(6)}$ for case W800 when t_A is doubled is considered as well. See appendix C.

Higher modes

The higher modes involve the higher-order harmonics of the organised motions discussed thus far as well as the turbulent fluctuations. This makes the analysis of the subsequent POD modes increasingly challenging since every mode now has signals with several frequencies, and possibly involves multiple physical phenomena. See figure 9.

In the remaining part of the paper, our attention is redirected to the identification of vortical structures and their morphological characterisation. The vortex detection is based upon reconstructed 3-D velocity fields consisting only of the most energetic higher POD modes. Expressed in a different manner, at a

https://doi.org/10.1017/flo.2023.26 Published online by Cambridge University Press

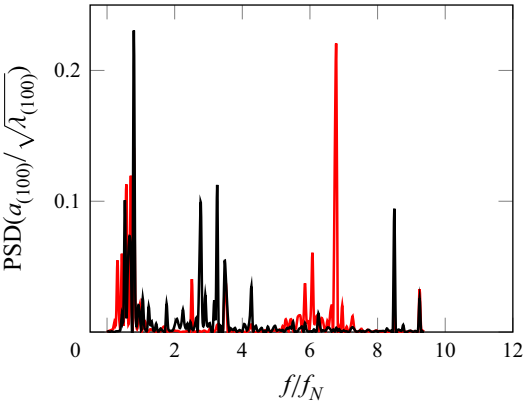

Figure 9. *The PSD corresponding to the normalised coefficient for mode 100. Here, f_N represents the impeller frequency in revolutions per second. Colours black and red correspond to cases W800 and C800, respectively. See table 2.*

given time t, $\boldsymbol{u}$ may be approximated as

$$\boldsymbol{u} \approx \sum_{k=1}^{r} a_{(k)}\boldsymbol{\phi}_{(k)} \equiv \underbrace{a_{(1)}\boldsymbol{\phi}_{(1)}}_{\text{(i)}} + \underbrace{\sum_{k=2}^{11} a_{(k)}\boldsymbol{\phi}_{(k)}}_{\text{(ii)}} + \underbrace{\sum_{k=12}^{r} a_{(k)}\boldsymbol{\phi}_{(k)}}_{\text{(iii)}}, \tag{4.1}$$

and the identification of vortices is based on term (iii). Considering the observations made through § 4, terms (i), (ii) and (iii) of (4.1) seem to represent (for the most part): the mean, periodic and fluctuating components of $\boldsymbol{u}$ according to Hussain & Reynolds's (1970) triple decomposition. Here, the upper limit r is set to capture (at least) ≈95 % of the total KE. Thus, the POD reconstruction is truncated at mode 130 which corresponds to $k/m \approx 0.3$ (see figure 2*b*). The reasoning for truncating the linear expansion at $r = 130$ is that within this range a significant amount of KE has already been captured and afterwards, the decay in the energy content is even slower. For example, for case W800 one captures 99 % of the total energy content only after keeping more than the first 300 modes. Indeed, one of the weaknesses of POD is that it is not always clear how many POD modes should be kept, and there are many different truncation criteria (Taira et al., 2017).

4.2. Vortical structures

The identification and morphological characterisation of vortices related to turbulence proceed as follows.

(i) The vortex criterion is computed. At a given instant, based on the approximation to the fluctuating velocity field, i.e. term (iii) of (4.1), the 3-D $Q_\star$ field is computed according to (3.6).

(ii) The vortex criterion is normalised to account for inhomogeneity in the flow. The 3-D $Q_\star$ field is normalised by its root mean square. The idea of using a statistical indicator of the turbulent structure concept to account for inhomogeneity in the flow started with Nagaosa and Handler (2003) and has been implemented in several works (see e.g. Arosemena, Andersson, Andersson, & Solsvik, 2021; del Álamo, Jiménez, Zandonade, & Moser, 2006; Hwang & Sung, 2018; Lozano-Durán, Flores, & Jiménez, 2012).

(iii) The normalised criterion is thresholded to identify the vortical structures. Regions of connected grid points where the normalised $Q_\star$-criterion is ≥1 are recognised as individual vortices. Here, connectivity is defined by the six orthogonal nearest neighbours of each grid point and the

https://doi.org/10.1017/flo.2023.26 Published online by Cambridge University Press

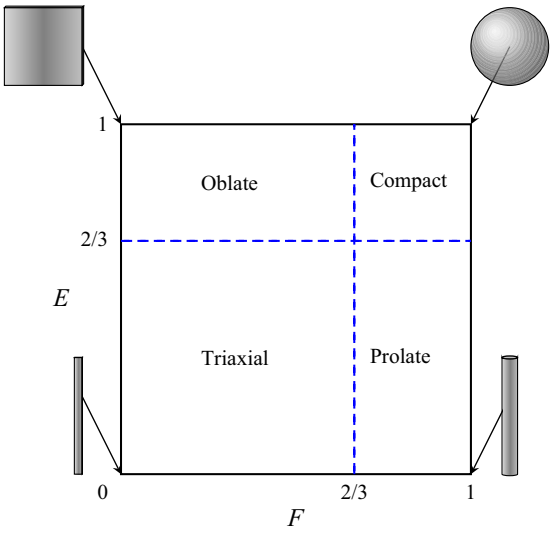

Figure 10. *Zingg's (1935) diagram for shape classification of objects according to their elongation E and flatness F parameters. Corners also illustrate extreme cases discussed in Moisy and Jiménez (2004): ribbons* $(0, 0)$*, sheets* $(0, 1)$*, tubes* $(1, 0)$ *and spheres* $(1, 1)$*. Reprinted from Arosemena et al. (2022), with permission of AIP Publishing.*

threshold is chosen considering the percolation crisis analysis performed by Arosemena et al. (2022). Also, it is worth mentioning that as in Arosemena et al. (2022) and due to the computational cost, a sensitivity analysis to the threshold selected is not performed. Nonetheless, based on previous studies (see e.g. Arosemena et al., 2021; Cheng, Li, Lozano-Durán, & Liu, 2020) and for threshold values larger than that where the percolation transition occurs, it is deemed probable that consistent trends in the results will be observed when changing the threshold value to another one differing by less than an order of magnitude.

(iv) The identified vortices are characterised according to statistics of shape-related parameters. Here, the shape of a vortical structure is determined by its maximum projection sphericity $\Phi_p = [d_S^2/(d_L d_I)]^{1/3}$ (Sneed & Folk, 1958), and its elongation $E = d_I/d_L$ and flatness $F = d_S/d_I$ parameters (Zingg, 1935). Here Φ_p represents the ratio of maximum projection area of a sphere having the same volume as the structure to the maximum projection area of the structure. Thus, Φ_p has a maximum of 1 for perfect spheres. On the other hand, the two aspect ratios (F, E) can be used to classify a structure in terms of its shape (see figure 10). Note that d_S, d_I and d_L are the shortest, intermediate and largest lengths of the oriented bounding box of a given structure. The boxes are computed by principal components analysis (see e.g. Jolliffe, 2002).

Figures 11(a) and 11(b) display the vortical structures identified by the above procedure for cases W800 and C800, respectively. The rendering takes place in the vicinity of the impeller (not shown in the figure) and for an instantaneous POD reconstruction based on term (iii) of (4.1). As can be seen, the vortices visually appear mostly as tubular structures. It is also interesting to note that the population of structures diminishes for the 0.2 wt% CMC case, as expected for the case having a lower Reynolds number and exhibiting shear-thinning fluid behaviour.

Regarding the shape-related parameters, figures 11(c) and 11(d) show the cumulative distribution function (CDF) of Φ_p and the joint CDF (JCDF) of F and E, respectively, for cases W800 and C800. Figure 11(c,d) also shows the results of Arosemena et al. (2022). As seen from figure 11(c), the probability of the identified vortices being non-spherical is above 90 %; i.e. CDF($\Phi_p \leq 0.9$) > 0.9 for both cases. This result is larger than CDF($\Phi_p \leq 0.9$) ≈ 0.8 reported by Arosemena et al. (2022)

https://doi.org/10.1017/flo.2023.26 Published online by Cambridge University Press

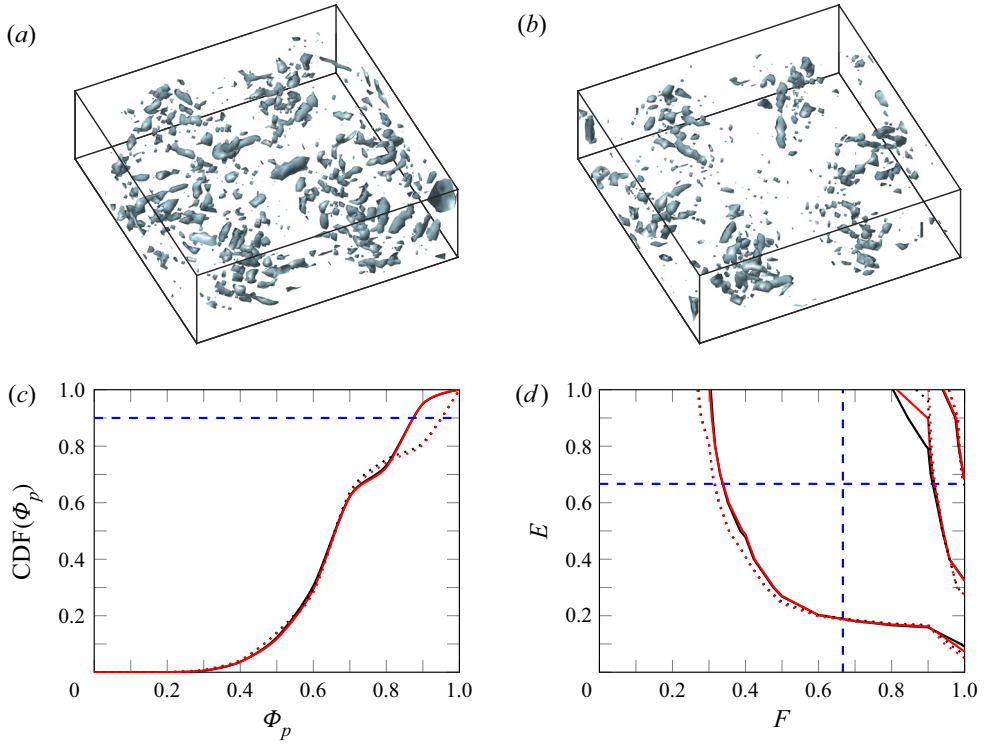

Figure 11. *Vortical structures based on POD reconstruction to approximate the fluctuating velocity field, and statistics of shape-related parameters. Isosurfaces of normalised $Q_\star$-criterion = 1 in the vicinity of the impeller, at a given instant, and for cases (a) W800 and (b) C800. Plots of (c) CDF(Φ_p) and (d) JCDF(F, E). In (c,d), continuous and dotted line styles correspond to the data of this work and that of Arosemena et al. (2022), whilst colours black and red correspond to cases W800 and C800, respectively. See table 2. Additionally, in (c), the dashed blue line marks CDF(Φ_p) = 0.9, whereas in (d), the blue lines mark the limits for shape classification (see figure 10). Also, in (d), the levels represented contain 99 %, 70 % and 30 % of the data.*

where the identification of vortices is based upon the instantaneous velocity field, instead of a POD reconstruction for the fluctuating velocity component. In addition, figure 11(*d*) reveals that about 70 % of identified structures are likely to fall into the compact and prolate categories whereas just 30 % of them fall into the compact category alone. This result is consistent with the finding of Arosemena et al. (2022), albeit in the latter the contour corresponding to 30 % of the data is slightly closer to the limit for perfect spheres (see figure 10). It is also interesting to observe that the contours of JCDF(F, E) capturing 70 % and 30 % of the data are for a very narrow range of large F values, i.e. $0.8 \leq F \leq 1$ and $0.9 \leq F \leq 1$, respectively. This finding further strengthens the argument in favour of tube-like vortices of different lengths being detected, instead of spherical ones.

5. Concluding remarks

In this work, POD is performed over instantaneous velocity fields obtained from the LES of an 11 l, baffled, stirred tank operating with a Rushton-type impeller at 800 r.p.m., and where the working fluid is either water or a 0.2 wt% CMC solution (Arosemena et al., 2022). The most energetic modes and their corresponding temporal coefficients are investigated. In addition, a POD reconstruction of the higher modes is carried out with the purpose of approximating the fluctuating velocity field and subsequently

https://doi.org/10.1017/flo.2023.26 Published online by Cambridge University Press

to explore the shape of vortices related to turbulence in the stirred vessel. Vortical structures are extremely important because of their role in mixing, and (potentially) in the breakup and coalescence of dispersed fluid particles. More specifically, the focus in their morphological characterisation is due to the fact that many phenomenological models for the breakage and coalescence of fluid particles (see e.g. Liao & Lucas, 2009, 2010; Solsvik et al., 2013) are based on several assumptions, including their interaction with vortices having comparable size and being of spherical shape. The identification of vortical structures is achieved through an objective version of the traditional Q-criterion (Hunt et al., 1988) which is normalised to also take into account the inhomogeneity in the rotating flow. On the other hand, the morphological classification of the identified structures is made thanks to statistics of their shape-related parameters, maximum projection sphericity and aspect ratios.

Findings of this paper include the following:

(i) It seems promising to implement the POD technique with the purpose of decomposing a 3-D flow field into its mean, and most energetic periodic and fluctuating components according to Hussain & Reynolds's (1970) triple decomposition.
(ii) Vortices associated with the fluctuating velocity field are mostly tubular structures.

Finding (i) appears to be valid regardless of the working fluid rheology, consistent with earlier POD analyses based on two-dimensional velocity fields (Gabelle, Morchain, Anne-Archard, Augier, & Liné, 2013; Liné et al., 2013). Likewise, as recognised by Moreau and Liné (2006), finding (i) signifies that one would be able to get the periodic component of the flow without the necessity of phased measurements. More importantly, this finding opens the window for reduced-order modelling of the organised structures arising due to periodic motions in the tank: trailing vortices and macroinstabilities. Previous works have considered low-order representations for these organised motions by approximating the corresponding temporal coefficients with sinusoidal functions (Doulgerakis et al. (2009); Ducci, Doulgerakis, and Yianneskis (2008), Doulgerakis et al. (2011) and Gabelle et al. (2013), to list a few). However, more generally, one can do a Galerkin projection of the momentum equation onto these POD modes to obtain a low-dimensional model for their coefficients (see e.g. Smith et al., 2005). Once the reduced-order model is solved, it would then be possible to predict the dynamical behaviour of these periodic structures, and thus better use these highly energetic regions for purposes such as mixing enhancement. The advantage of following the more general approach is that one is not restricted to simple periodic motion. Meanwhile, finding (ii) suggests that as starting point for the modelling of breakage and coalescence of fluid particles in stirred tanks and based on their interaction with vortices, it is more reasonable to assume that the latter are cylindrical structures rather than spherical. Moreover, this observation is more in line with our understanding about vortices in turbulent flows (see e.g. Davidson (2015), § 5.3). Lastly, through this work and as expected, an overall attenuation of the swirling-like motions (e.g. circulation loops, trailing vortices and vortical structures associated with turbulence) is observed with shear-thinning rheology compared with the Newtonian case.

Finally, it is worth mentioning some limitations of the present investigation. Firstly, since POD is performed over data obtained from LES, none of the higher-order modes are representative of the dissipative scales. Information about the small-scale motions would be particularly useful for improvement of chemically reactive systems and mass transfer. Secondly, the different periodic motions in the tank present different time scales and for proper characterisation of some of them one may require larger simulation times and a complementary dataset with samples collected using a smaller sampling frequency. For example, precessional macroinstabilities in the turbulent regime have a normalised frequency of $f/f_N \approx 0.02$ (Nikiforaki et al., 2003) which is about 300 times smaller than that characteristic of the trailing vortices, i.e. $f/f_N \approx 6$. Thirdly, the standard POD does not ensure temporal coherence and, as seen in § 4.1, it may result in temporal signals with mixed frequencies. This is obviously problematic when considering higher-order modes since it is difficult to separate the higher-order harmonics corresponding to the organised motion from turbulence, yet it may also represent an issue in the case of the lower-order ones when physical phenomena, taking place at different frequencies, appear in the same mode. In such cases, it is rather difficult to determine if a structure is evolving into another as it moves in

https://doi.org/10.1017/flo.2023.26 Published online by Cambridge University Press

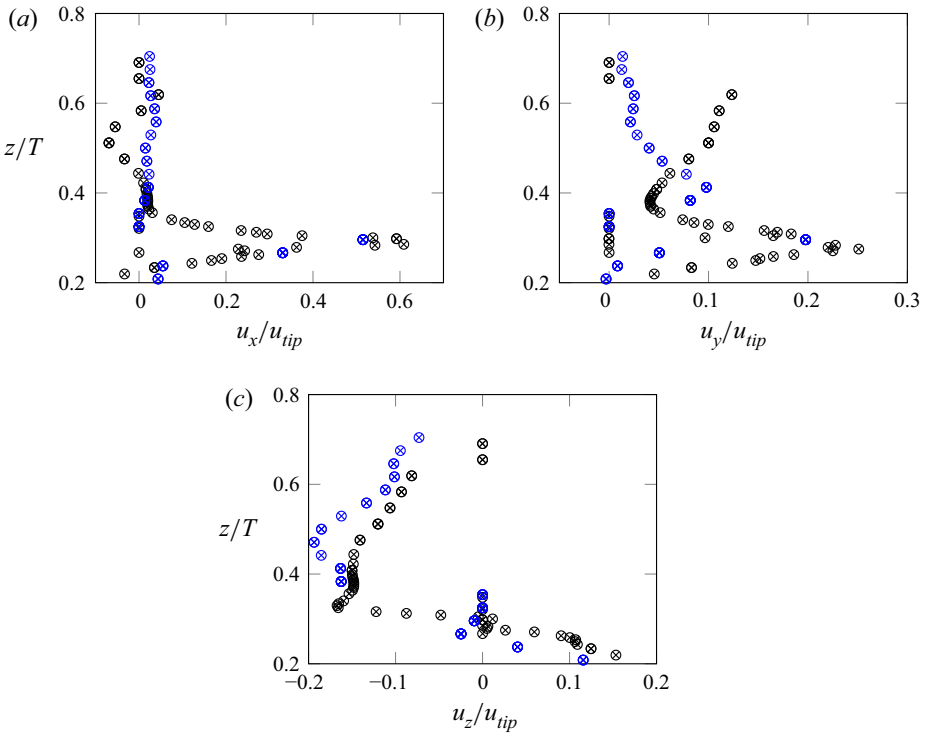

Figure 12. *Normalised instantaneous velocity components at different axial positions, z/T: (a) u_x/u_{tip}, (b) u_y/u_{tip} and (c) u_z/u_{tip}. Circle and cross markers are used for the original and the interpolated velocity values, respectively. Black and blue colours correspond to the nearest points to $x/(D/2), y/(D/2) = 0, 0.6$ and $0, 1.25$, respectively. Here, the data correspond to case W800. See table 2.*

space or if both structures have similar energy content and simply end sharing the same mode (Mendez, Balabane, & Buchlin, 2019). Here, a better approach could be one that extracts spatio-temporal coherence such as spectral POD (see e.g. Schmidt & Colonius, 2020; Towne, Schmidt, & Colonius, 2018) or another where there is some trade-off between energy optimality and spectral purity such as multi-scale POD (Mendez et al., 2019). Lastly, it is important to keep in mind that POD is the optimal linear decomposition when one is interested in capturing the energy of the original data, yet it is not when the interest resides in another property. Furthermore, turbulence is certainly highly nonlinear, and a different approach may be more appropriate. For instance, consider the nonlinear wavelet decomposition (see e.g. Farge & Schneider, 2006), or more recent data-driven methods, such as convolutional neural networks (CNNs) POD (see Guastoni et al., 2021; Güemes, Discetti, & Ianiro, 2019; Nakamura, Fukami, & Fukagata, 2022). A CNN POD method considers the same spatial basis as traditional POD; however, the time coefficients are estimated using a CNN, making it able to account for nonlinear features in the flow.

Supplementary material. Raw data are available from the authors.

Funding statement. This work was supported by the Research Council of Norway (RCN, grant no. 274398).

Declaration of interests. The authors report no conflict of interest.

Appendix A. Interpolation

Figure 12(*a–c*) compares a randomly selected velocity field for case W800, taken after approximately 13.33 impeller revolutions from the first saved snapshot, with its Sibson interpolation. The figure

https://doi.org/10.1017/flo.2023.26 Published online by Cambridge University Press

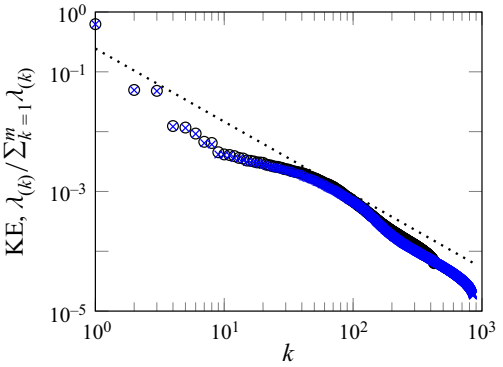

Figure 13. *Fraction of total KE versus mode number, k, for case W800. See table 2. Markers in black and blue colours correspond to a total number of modes, m, equal to* 426 *and to* 851*, respectively. Dotted line represents the* $-11/9$ *power law (Knight & Sirovich, 1990).*

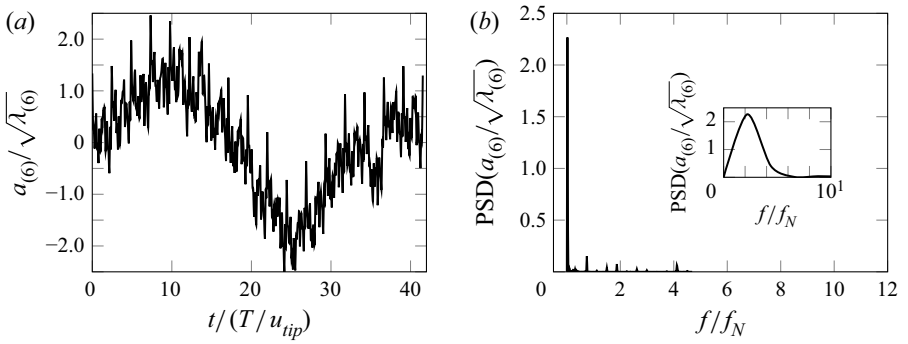

Figure 14. *Temporal coefficients of the sixth POD mode, case W800: (a) normalised temporal coefficient and (b) PSD corresponding to the normalised coefficient. Total sampling time,* t_A*, is twice that listed in table 2.*

displays the x-, y- and z-instantaneous velocity components, u_x, u_y and u_z, respectively, for different axial positions in the vicinity of the impeller. As can be seen, there is very good agreement between the original field and its interpolation.

Appendix B. Sensitivity to the number of considered snapshots

Figure 13 compares the fraction of total KE contained in a given k-mode when $m = 426$ with the fraction when m is doubled, for case W800 and for the same t_A. See table 2. As can be seen, the profiles are very similar, especially for the modes containing most of the total KE.

Appendix C. Precessional macroinstabilities

Figure 14(a) shows the temporal signal of mode 6 for case W800 when $m = 426$, and t_A and Δt are doubled. See table 2. From this figure, one observes what appears to be a full cycle of the precessional motion. Of course, for proper study of precessional macroinstabilities, a larger t_A – covering several full cycles of the precessional motion – is required.

https://doi.org/10.1017/flo.2023.26 Published online by Cambridge University Press

References

Arosemena, A.A., Ali, H., & Solsvik, J. (2022). Characterization of vortical structures in a stirred tank. *Physics of Fluids*, *34*, 0083843.

Arosemena, A.A., Andersson, R., Andersson, H.I., & Solsvik, J. (2021). Effects of shear-thinning rheology on near-wall turbulent structures. *Journal of Fluid Mechanics*, *925*, A37.

Bakewell, H.P., & Lumley, J.L. (1967). Viscous sublayer and adjacent wall region in turbulent pipe flow. *Physics of Fluids*, *10*, 1880–1889.

Başbuğ, S., Papadakis, G., & Vassilicos, J.C. (2018a). Reduced power consumption in stirred vessels by means of fractal impellers. *American Institute of Chemical Engineers Journal*, *64*, 1485–1499.

Başbuğ, S., Vassilicos, J.C., & Papadakis, G. (2018b). Reduced mixing time in stirred vessels by means of irregular impellers. *Physical Review Fluids*, *3*, 084502.

Berkooz, G., Holmes, P., & Lumley, J.L. (1993). The proper orthogonal decomposition in the analysis of turbulent flows. *Annual Review of Fluid Mechanics*, *25*, 539–575.

Bouremel, Y., Yianneskis, M., & Ducci, A. (2009). On the utilisation of vorticity and strain dynamics for improved analysis of stirred processes. *Chemical Engineering Research and Design*, *87*, 377–385.

Cantwell, B.J. (1981). Organized motion in turbulent flow. *Annual Review of Fluid Mechanics*, *13*, 457–515.

Chakraborty, P., Balachandar, S., & Adrian, R. (2005). On the relationships between local vortex identification schemes. *Journal of Fluid Mechanics*, *535*, 189–214.

Charalambidou, A.-D., Micheletti, M., & Ducci, A. (2023). Study of trailing vortices and impeller jet instabilities of a flat blade impeller in small-scale reactors. *American Institute of Chemical Engineers Journal*, *69*, e17842.

Cheng, C., Li, W., Lozano-Durán, A., & Liu, H. (2020). On the structure of streamwise wall-shear stress fluctuations in turbulent channel flows. *Journal of Fluid Mechanics*, *903*, A29.

Chhabra, R.P., & Richardson, J.F. (2008). Liquid mixing. In *Non-Newtonian flow and applied rheology* (pp. 376–461). Oxford, UK: Butterworth-Heinemann.

Chong, M.S., Perry, A.E., & Cantwell, B.J. (1990). A general classification of three–dimensional flow fields. *Physics of Fluids A*, *2*(5), 765–777.

Davidson, P.A. (2015). *Turbulence: An introduction for scientists and engineers*. Oxford, UK: Oxford University Press.

de Lamotte, A., Delafosse, A., Calvo, S., & Toye, D. (2018). Identifying dominant spatial and time characteristics of flow dynamics within free-surface baffled stirred-tanks from CFD simulations. *Chemical Engineering Science*, *192*, 128–142.

del Álamo, J.C., Jiménez, J., Zandonade, P., & Moser, R.D. (2006). Self-similar vortex clusters in the turbulent logarithmic region. *Journal of Fluid Mechanics*, *561*, 329–358.

Doulgerakis, Z., Yianneskis, M., & Ducci, A. (2009). On the interaction of trailing and macro-instability vortices in a stirred vessel-enhanced energy levels and improved mixing potential. *Chemical Engineering Research and Design*, *87*, 412–420.

Doulgerakis, Z., Yianneskis, M., & Ducci, A. (2011). On the manifestation and nature of macroinstabilities in stirred vessels. *American Institute of Chemical Engineers Journal*, *57*, 2941–2954.

Ducci, A., Doulgerakis, Z., & Yianneskis, M. (2008). Decomposition of flow structures in stirred reactors and implications for mixing enhancement. *Industrial & Engineering Chemistry Research*, *47*, 3664–3676.

Ducci, A., & Yianneskis, M. (2007). Vortex tracking and mixing enhancement in stirred processes. *American Institute of Chemical Engineers Journal*, *53*, 305–315.

Epps, B.P. (2017). Review of vortex identification methods. In *55th American Institute of Aeronautics and Astronautics Aerospace Sciences Meeting* (AIAA 2017-0989). American Institute of Aeronautics and Astronautics.

Escudié, R., Bouyer, D., & Liné, A. (2004). Characterization of trailing vortices generated by a Rushton turbine. *American Institute of Chemical Engineers Journal*, *50*, 75–85.

Escudié, R., & Liné, A. (2003). Experimental analysis of hydrodynamics in a radially agitated tank. *American Institute of Chemical Engineers Journal*, *49*, 585–603.

Fan, Y., Sun, J., Jin, J., Sun, K., Zhang, H., Chen, W., & Li, Y. (2022). Effects of baffle on flow structure and cyclic variation in stirred tanks with rushton turbine. *American Institute of Physics Advances*, *12*, 015202.

Farge, M., & Schneider, K. (2006). Wavelets: Application to turbulence. In J.P. Françoise, G.L. Naber, & T.S. Tsun (Eds.), *Encyclopedia of mathematical physics* (pp. 408–420). Academic Press.

Gabelle, J.-C., Morchain, J., Anne-Archard, D., Augier, F., & Liné, A. (2013). Experimental determination of the shear rate in a stirred tank with a non-Newtonian fluid: Carbopol. *American Institute of Chemical Engineers Journal*, *59*, 2251–2266.

Gabelle, J.-C., Morchain, J., & Liné, A. (2017). Kinetic energy transfer between first proper orthogonal decomposition modes in a mixing tank. *Chemical Engineering & Technology*, *40*, 927–937.

Galletti, C., Paglianti, A., & Yianneskis, M. (2005). Observations on the significance of instabilities turbulence and intermittent motions on fluid mixing processes in stirred reactors. *Chemical Engineering Science*, *60*, 2317–2331.

Guastoni, L., Güemes, A., Ianiro, A., Discetti, S., Schlatter, P., Azizpour, H., & Vinuesa, R. (2021). Convolutional-network models to predict wall-bounded turbulence from wall quantities. *Journal of Fluid Mechanics*, *928*, A27.

Güemes, A., Discetti, S., & Ianiro, A. (2019). Sensing the turbulent large-scale motions with their wall signature. *Physics of Fluids*, *31*, 125112.

https://doi.org/10.1017/flo.2023.26 Published online by Cambridge University Press

Günther, T., Gross, M., & Theisel, H. (2017). Generic objective vortices for flow visualization. *Association for Computing Machinery Transactions on Graphics*, *36*, 1–11.

Günther, T., Schulze, M., & Theisel, H. (2016). Rotation invariant vortices for flow visualization. *Institute of Electrical and Electronics Engineers Transactions on Visualization and Computer Graphics*, *22*, 817–826.

Haller, G. (2005). An objective definition of a vortex. *Journal of Fluid Mechanics*, *525*, 1–26.

Haller, G. (2021). Can vortex criteria be objectivized? *Journal of Fluid Mechanics*, *908*, A25.

Haller, G., Hadjighasem, A., Farazmand, M., & Huhn, F. (2016). Defining coherent vortices objectively from the vorticity. *Journal of Fluid Mechanics*, *795*, 136–173.

Hasal, P., Montes, J.-L., Boisson, H.-C., & Fořt, I. (2000). Macro-instabilities of velocity field in stirred vessel: Detection and analysis. *Chemical Engineering Science*, *55*, 391–401.

Holmes, P., Lumley, J.L., Berkooz, G., & Rowley, C.W. (2012). *Turbulence, coherent structures, dynamical systems and symmetry*. Cambridge, UK: Cambridge University Press.

Hunt, J.C.R., Wray, A.A., & Moin, P. (1988). Eddies, streams and convergence zones in turbulent flows. In *Studying Turbulence Using Numerical Simulation Databases, Proceedings of the Summer Program* (pp. 193–208). Center for Turbulence Research.

Hussain, A.K.M.F., & Reynolds, W.C. (1970). The mechanics of an organized wave in turbulent shear flow. *Journal of Fluid Mechanics*, *41*, 241–258.

Hwang, J., & Sung, H. (2018). Wall-attached structures of velocity fluctuations in a turbulent boundary layer. *Journal of Fluid Mechanics*, *856*, 958–983.

Irgens, F. (2014). Generalized Newtonian fluids. In *Rheology and non-Newtonian fluids* (pp. 113–125). Cham, Switzerland: Springer.

Janiga, G. (2019). Large-eddy simulation and 3D proper orthogonal decomposition of the hydrodynamics in a stirred tank. *Chemical Engineering Science*, *201*, 132–144.

Jeong, J., & Hussain, F. (1995). On the identification of a vortex. *Journal of Fluid Mechanics*, *177*, 69–94.

Jiménez, J. (2018). Coherent structures in wall-bounded turbulence. *Journal of Fluid Mechanics*, *842*, P1.

Jolliffe, I.T. (2002). *Principal component analysis*. New York, NY: Springer.

Knight, B., & Sirovich, L. (1990). Kolmogorov inertial range for inhomogeneous turbulent flows. *Physical Review Letters*, *65*, 1356–1359.

Kresta, S.M., & Brodkey, R.S. (2004). Turbulence in mixing applications. In E.L. Paul, V.A. Atiemo-Obeng, & S.M. Kresta (Eds.), *Handbook of industrial mixing: Science and practice* (pp. 44–45). John Wiley & Sons.

Küchemann, D. (1965). Report on the I.U.T.A.M. symposium on concentrated vortex motions in fluids. *Journal of Fluid Mechanics*, *21*, 1–20.

Liao, Y., & Lucas, D. (2009). A literature review of theoretical models for drop and bubble breakup in turbulent dispersions. *Chemical Engineering Science*, *64*, 3389–3406.

Liao, Y., & Lucas, D. (2010). A literature review on mechanisms and models for the coalescence process of fluid particles. *Chemical Engineering Science*, *65*, 2851–2864.

Liné, A., Gabelle, J.-C., Morchain, J., Anne-Archard, D., & Augier, F. (2013). On POD analysis of PIV measurements applied to mixing in a stirred vessel with a shear thinning fluid. *Chemical Engineering Research and Design*, *91*, 2073–2083.

Liu, C., Gao, Y., Tian, S., & Dong, X. (2018). Rortex–A new vortex vector definition and vorticity tensor and vector decompositions. *Physics of Fluids*, *30*, 035103.

Liu, C., Wang, Y., Yang, Y., & Duan, Z. (2016). New omega vortex identification method. *Science China Physics, Mechanics & Astronomy*, *59*, 684711.

Liu, J., Gao, Y., & Liu, C. (2019a). An objective version of the rortex vector for vortex identification. *Physics of Fluids*, *31*, 065112.

Liu, J., Gao, Y., Wang, Y., & Liu, C. (2019b). Objective omega vortex identification method. *Journal of Hydrodynamics*, *31*, 455–463.

Lozano-Durán, A., Flores, O., & Jiménez, J. (2012). The three-dimensional structure of momentum transfer in turbulent channels. *Journal of Fluid Mechanics*, *694*, 100–130.

Lumley, J.L. (1967). The structure of inhomogeneous turbulence. In A.M. Yaglom & V.I. Tatarsky (Eds.), *Atmospheric turbulence and radio wave propagation* (pp. 166–178).

Lumley, J.L. (1970). *Stochastic tools in turbulence*. London, UK: Academic Press.

Luo, J.Y., Issa, R.I., & Gosman, A.D. (1994). Prediction of impeller induced flows in mixing vessels using multiple frames of reference. In *Proceedings of 8th European Conference on Mixing* (pp. 549–556). Institution of Chemical Engineers.

Mayorga, C., Morchain, J., & Liné, A. (2022). Reconstruction of the 3D hydrodynamics in a baffled stirred tank using proper orthogonal decomposition. *Chemical Engineering Science*, *248*, 117220.

Mendez, M.A., Balabane, M., & Buchlin, J.-M. (2019). Multi-scale proper orthogonal decomposition of complex fluid flows. *Journal of Fluid Mechanics*, *870*, 988–1036.

Metzner, A.B., & Otto, R.E. (1957). Agitation of non-Newtonian fluids. *American Institute of Chemical Engineers Journal*, *3*, 3–10.

Mikhaylov, K., Rigopoulos, S., & Papadakis, G. (2021). Reconstruction of large-scale flow structures in a stirred tank from limited sensor data. *American Institute of Chemical Engineers Journal*, *67*, 10.

https://doi.org/10.1017/flo.2023.26 Published online by Cambridge University Press

Mikhaylov, K., Rigopoulos, S., & Papadakis, G. (2023a). Decomposition of power number in a stirred tank and real time reconstruction of 3D large-scale flow structures from sparse pressure measurements. *Chemical Engineering Science*, *279*, 118881.

Mikhaylov, K., Rigopoulos, S., & Papadakis, G. (2023b). Three-dimensional characterisation of macro-instabilities in a turbulent stirred tank flow and reconstruction from sparse measurements using machine learning methods. *Chemical Engineering Research and Design*, *196*, 276–296.

Moisy, F., & Jiménez, J. (2004). Geometry and clustering of intense structures in isotropic turbulence. *Journal of Fluid Mechanics*, *513*, 111–133.

Moreau, J., & Liné, A. (2006). Proper orthogonal decomposition for the study of hydrodynamics in a mixing tank. *American Institute of Chemical Engineers Journal*, *52*, 2651–2655.

Murthy, J.Y., Mathur, S.R., & Choudhury, D. (1994). CFD simulation of flows in stirred tank reactors using a sliding mesh technique. In *Proceedings of 8th European Conference on Mixing* (pp. 341–348). Institution of Chemical Engineers.

Nagaosa, R., & Handler, R.A. (2003). Statistical analysis of coherent vortices near a free surface in a fully developed turbulence. *Physics of Fluids*, *15*, 375–394.

Nakamura, T., Fukami, K., & Fukagata, K. (2022). Identifying key differences between linear stochastic estimation and neural networks for fluid flow regressions. *Scientific Reports*, *12*, 3726.

Nikiforaki, L., Montante, G., Lee, K.C., & Yianneskis, M. (2003). On the origin, frequency and magnitude of macro-instabilities of the flows in stirred vessels. *Chemical Engineering Science*, *58*, 2937–2949.

Park, S.W., Linsen, L., Kreylos, O., Owens, J.D., & Hamann, B. (2006). Discrete Sibson interpolation. *Institute of Electrical and Electronics Engineers Transactions on Visualization and Computer Graphics*, *12*, 243–253.

Pope, S.B. (2000). *Turbulent flows*. Cambridge, UK: Cambridge University Press.

Press, W.H., Teukolsky, S.A., Vetterling, W.T., & Flannery, B.P. (2007). *Numerical recipes: The art of scientific computing*. Cambridge, UK: Cambridge University Press.

Raju, R., Balachandar, S., Hill, D., & Adrian, R. (2005). Reynolds number scaling of flow in a stirred tank with Rushton turbine. Part II–Eigen decomposition of fluctuation. *Chemical Engineering Science*, *60*, 3185–3198.

Roussinova, V., Kresta, S.M., & Weetman, R. (2003). Low frequency macroinstabilities in a stirred tank: Scale-up and prediction based on large eddy simulations. *Chemical Engineering Science*, *58*, 2297–2311.

Schmid, P.J. (2010). Dynamic mode decomposition of numerical and experimental data. *Journal of Fluid Mechanics*, *656*, 5–28.

Schmid, P.J., Violato, D., & Scarano, F. (2012). Decomposition of time-resolved tomographic PIV. *Experiments in Fluids*, *52*, 1567–1579.

Schmidt, O.T., & Colonius, T. (2020). Guide to spectral proper orthogonal decomposition. *American Institute of Aeronautics and Astronautics Journal*, *58*, 1023–1033.

Sharp, K.V., & Adrian, R.J. (2001). PIV study of small-scale flow structure around a Rushton turbine. *American Institute of Chemical Engineers Journal*, *47*, 766–778.

Sibson, R. (1981). A brief description of natural neighbor interpolation. In V. Barnett (Ed.), *Interpreting multivariate data* (pp. 21–36). Wiley.

Sirovich, L. (1987). Turbulence and the dynamics of coherent structures. Part I: Coherent structures. *Quarterly of Applied Mathematics*, *45*, 561–571.

Smith, T.R., Moehlis, J., & Holmes, P. (2005). Low-dimensional modelling of turbulence using the proper orthogonal decomposition: A tutorial. *Nonlinear Dynamics*, *41*, 275–307.

Sneed, E.D., & Folk, R.L. (1958). Pebbles in the lower Colorado river, Texas: A study in particle morphogenesis. *The Journal of Geology*, *66*, 114–150.

Solsvik, J., Tangen, S., & Jakobsen, H.A. (2013). On the constitutive equations for fluid particle breakage. *Reviews in Chemical Engineering*, *29*, 241–356.

Taira, K., Brunton, S.L., Dawson, S.T.M., Rowley, C.W., Colonius, T., McKeon, B.J., . . . Ukeiley, L.S. (2017). Modal analysis of fluid flows: an overview. *American Institute of Aeronautics and Astronautics Journal*, *55*, 4013–4041.

Tian, S., Gao, Y., Dong, X., & Liu, C. (2018). Definitions of vortex vector and vortex. *Journal of Fluid Mechanics*, *564*, 57–103.

Towne, A., Schmidt, O.T., & Colonius, T. (2018). Spectral proper orthogonal decomposition and its relationship to dynamic mode decomposition and resolvent analysis. *Journal of Fluid Mechanics*, *847*, 821–867.

van Oudheusden, B.W., Scarano, F., van Hinsberg, N.P., & Watt, D.W. (2005). Phase-resolved characterization of vortex shedding in the near wake of a square-section cylinder at incidence. *Experiments in Fluids*, *39*, 86–98.

Van't Riet, K., & Smith, J.M. (1975). The trailing vortex system produced by Rushton turbine agitator. *Chemical Engineering Science*, *30*, 1093–1105.

Weiss, J. (2019). A tutorial on the proper orthogonal decomposition. In *2019 American Institute of Aeronautics and Astronautics Aviation Forum* (AIAA 2019-3333). American Institute of Aeronautics and Astronautics.

Zingg, T. (1935). *Beitrag zur schotteranalyse* (PhD thesis). ETH Zurich, Zurich, Switzerland.

Cite this article: Arosemena AA, Solsvik J (2023). Proper orthogonal decomposition modal analysis in a baffled stirred tank: a base tool for the study of structures. *Flow*, *3*, E32. doi:10.1017/flo.2023.26